ARTEMIS II: A Second-Generation Catalog of LASCO Coronal Mass Ejections Including Mass and Kinetic Energy

O. Floyd · P. Lamy · Y. Boursier · A. Llebaria

Abstract The ARTEMIS-I catalog of coronal mass ejections (CMEs) was initially developed on a first generation of low-resolution synoptic maps constructed from the SOHO/LASCO-C2 images of the K-corona and resulted in an online database listing all events detected since January 1996 (Boursier *et al.*, *Solar Phys.* **257**, 125, 2009). A new generation of synoptic maps with higher temporal (a factor of 1.5) and angular (a factor of 2.5) resolutions allowed us to reconsider the question of CME detection and resulted in the production of a new catalog: ARTEMIS-II. The parameters estimated for each detected CME are still the date and time of appearance, the position angle, the angular width, and (when detected at several solar distances) the global and median velocities. The new synoptic maps correct for the limited number of velocity determinations reported in the ARTEMIS-I catalog. We now determine the propagation velocity of 79 % of detected CMEs instead of 30 % in the previous version. A final major improvement is the estimation of the mass and kinetic energy of all CMEs for which we could determine the velocity, that is ≈ 13 000 CMEs until December 2010. Individual comparisons of velocity determination of 23 CMEs for which a full three-dimensional kinematical solution has been published indicate that ARTEMIS-II performs extremely well except at the highest velocities, an intrinsic limitation of our method. Finally, individual comparisons of mass determination of seven CMEs for which a robust solution has been obtained from stereographic observations demonstrate the quality of the ARTEMIS-II results.

O. Floyd · P. Lamy (✉) · A. Llebaria
Laboratoire d'Astrophysique de Marseille, UMR 7326, CNRS/Université de Provence,
38 rue Frédéric Joliot-Curie, 13388 Marseille cedex 13, France
e-mail: philippe.lamy@oamp.fr

O. Floyd
e-mail: olivier.floyd@oamp.fr

A. Llebaria
e-mail: antoine.llebaria@oamp.fr

Y. Boursier
Aix-Marseille Université, CPPM, CNRS/IN2P3, UMR 6550, 13288 Marseille, France
e-mail: boursier@cppm.in2p3.fr

ⓐ Springer

Keywords Coronal mass ejections · Initiation and propagation

1. Introduction

Since their first detection by the OSO-7 spacecraft (Tousey, Howard, and Koomen, 1974), coronal mass ejections (CMEs, historically defined as transient events where coronal plasma is ejected by the Sun at velocities exceeding that of the local solar wind) have attracted considerable attention. These transient events play a major role in the dynamical evolution of the solar corona, and their interaction with the planets, especially the Earth, has led to the development of the new field of space-weather research. As observations accumulate with time, the inventory of CMEs has emerged as a basic tool for investigating their properties, for instance on a statistical basis. The advent of the highly sensitive *Large Angle Spectrometric COronagraph* (LASCO: Brueckner *et al.*, 1995), which is in nearly continuous operation since 1996, has resulted in the detection of thousands of coronal mass ejections, thus requiring special efforts for their inventory.

A first LASCO CME catalog was assembled by the Coordinated Data Analysis Workshop (CDAW) Data Center (currently online at http://cdaw.gsfc.nasa.gov/CME_list/), and relies on visual detection. Limitations and biases inherent in this method were soon realized, and the next-generation catalogs are all based on automatic detection:

- The Computer Aided CME Tracking catalog (CACTus: http://sidc.oma.be/cactus/) developed at the Royal Observatory of Belgium (Robbrecht and Berghmans, 2004; Robbrecht, Berghmans, and Van der Linden, 2009). It relies on the LASCO-C2 and -C3 data for the period April 1997 – March 2007. A new version has recently been released covering the period from April 1997 until now, but is not documented.
- The Solar Eruptive Event Detection System catalog (SEEDS: http://spaceweather.gmu.edu/seeds/) developed at the George Mason University (Olmedo *et al.*, 2005, 2008). It relies on the LASCO-C2 data from April 1997 until now.
- The catalog developed by Qu *et al.* (2006), no longer available online and limited to less than four years (2002 – 2006).
- The Automatic Recognition of Transient Events and Marseille Inventory from Synoptic maps catalog (ARTEMIS: http://lascor.oamp.fr/lasco/index.jsp) developed by our team at the Laboratoire d'Astrophysique de Marseille (Boursier *et al.*, 2009) and covering the period from June 1996 to December 2010.

The characteristic of the ARTEMIS catalog (hereafter referred to as ARTEMIS-I, to distinguish from the new-generation catalog ARTEMIS-II, which is the subject of this article) lies in using synoptic maps rather than coronal images, either original or transformed. The first-generation synoptic maps assembled at the Laboratoire d'Astrophysique de Marseille (LAM) were not specifically tailored to the detection of CMEs, however, but intended to provide global views of the corona and its activity. In fact, they did not take advantage of the full spatial and temporal resolutions of the LASCO-C2 images, in particular of the increased temporal cadence that was progressively implemented. With the growing realization that synoptic maps are a powerful tool for characterizing the corona and CMEs in particular, we decided to construct a completely new set of maps with the highest possible resolution allowed by the total number of C2 images. We anticipated that they would lead to improving the detection of CMEs and the estimation of their physical parameters. This article presents the results of this effort, which culminated in the production of the second-generation catalog of LASCO CMEs: ARTEMIS-II.

In Section 2, we briefly recall how the synoptic maps are constructed and emphasize the distinct features of the new high-definition (HD) maps. Section 3 starts with an overview of our method of detecting CMEs, explains how the original method was adapted to the HD synoptic maps, and then addresses the determination of their physical parameters. A specific development is presented for the mass, because this is the first time that this parameter is calculated from the synoptic maps. Some statistical results are presented in Section 4 to allow comparing the results of the two ARTEMIS catalogs also to other catalogs. We finally take advantage of the robust measurements obtained from stereographic observations of a few CMEs to assess the quality of the velocity and mass estimations of the ARTEMIS-II and other catalogs. We conclude in Section 5.

2. The LASCO Synoptic Maps

Synoptic maps of the K-corona radiance are constructed from time series of LASCO-C2 images (≥ 50 per day) first corrected for instrumental effects, and calibrated in units of mean solar radiance. The extensive correction of the raw images, the separation of the K-corona, and the generation of the synoptic maps implemented in the pipeline processing developed by the LASCO team at the Laboratoire d'Astrophysique de Marseille has been described by Saez *et al.* (2007) and Boursier *et al.* (2009). Our synoptic maps of the K-corona radiance corresponding to successive Carrington rotations [CR] as first introduced by Lamy, Llebaria, and Quemerais (2002) are non-standard because they simultaneously display both east and west limbs. Starting from the set of images of the K-corona radiance obtained at successive times during a given CR, they are converted from Cartesian to polar coordinates by extracting circular profiles at different radial distances from the center of the Sun. These profiles are then stacked and resampled uniformly with time by linear interpolation in a frame where the horizontal or x-axis represents time running from left to right (this is equivalent to the longitude of the central meridian of the Sun), and where the vertical or y-axis represents the solar polar angle running from $0°$ to $360°$ starting from the South Pole and increasing counterclockwise (instead of the latitude running from $-90°$ to $90°$ in the standard synoptic maps). Our synoptic maps are generated at radial distances in multiples of 0.5 R$_\odot$ inside the field-of-view of LASCO-C2 and range from 3 to 5.5 R$_\odot$.

The first generation of synoptic maps used to generate the ARTEMIS-I catalog were constructed from K-corona images resized to a common format of 512×512 pixels and transformed to polar coordinates with an angular step of $1°$. A uniform resampling with a time step of 27.3 days$/1000 = 39.3$ minutes was applied to remove the effect of irregular image acquisition. These maps therefore have a format of 1000 pixels in longitude and 360 pixels in solar polar angle.

The second generation of synoptic maps used to generate the ARTEMIS-II catalog were constructed from K-corona images resized to a common format of 512×512 pixels with two different angular steps: $0.4°$ for radial distances of 3 and 3.5 R$_\odot$ and $0.25°$ beyond. A uniform resampling with a time step of 27.3 days$/1440 = 27.3$ minutes was applied. These maps therefore have a format of 1440×900 pixels at radial distance of 3 and 3.5 R$_\odot$ and of 1440×1440 pixels at larger distances.

The temporal resolution therefore has increased because the time step decreased from 39 to 27 minutes, reflecting the variation of the monthly image rate displayed in Figure 1. The new resolution is now comparable to the average temporal cadence of the C2 images during the past 12 years, that is ≈ 24 minutes. An example of the difference between the two generations of synoptic maps is shown in Figure 2. The images of CMEs appear much
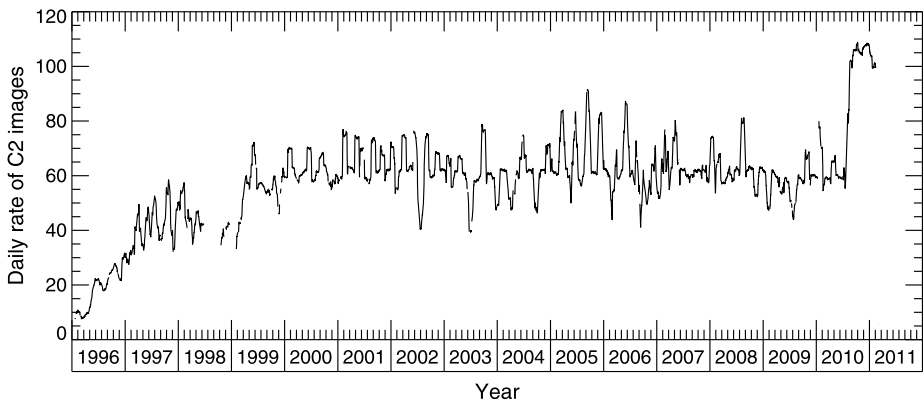
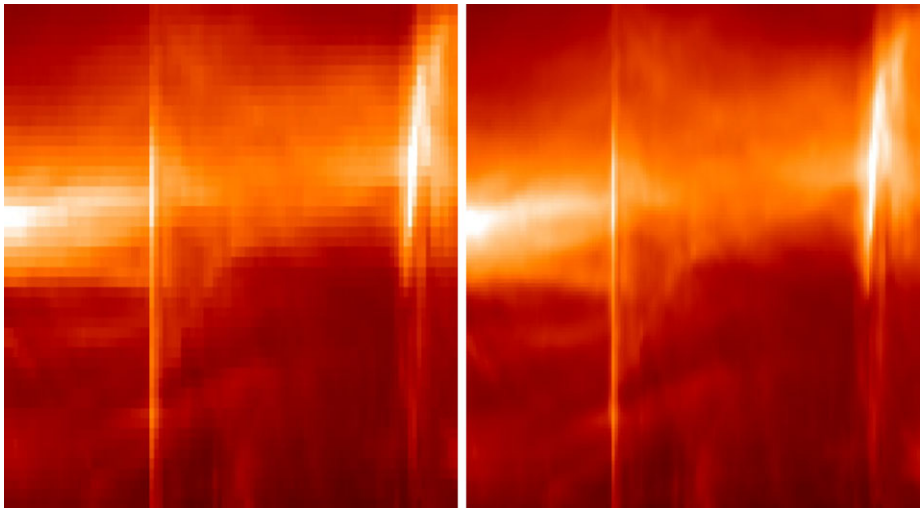**Figure 1** Monthly averaged daily rate of LASCO-C2 images from 1996 to 2010.

Figure 2 Enlarged subimages of low- (left panel) and high- (right panel) resolution synoptic maps illustrating the improved detection of CMEs (vertical streaks). Each subimage extends over 2.7 days (x-axis) and 50° (y-axis).

sharper on the new maps, which facilitates detecting as well as identifying them at various distances to estimate their velocity.

3. CME Detection Method

3.1. Overview of the Detection Method

The detection method implemented in the ARTEMIS-I catalog has already been described in detail (Boursier *et al.*, 2009). ARTEMIS-II is built with the same procedure, which consists of four steps: filtering, thresholding, segmenting, and merging with high-level knowledge, as illustrated in Figure 3.
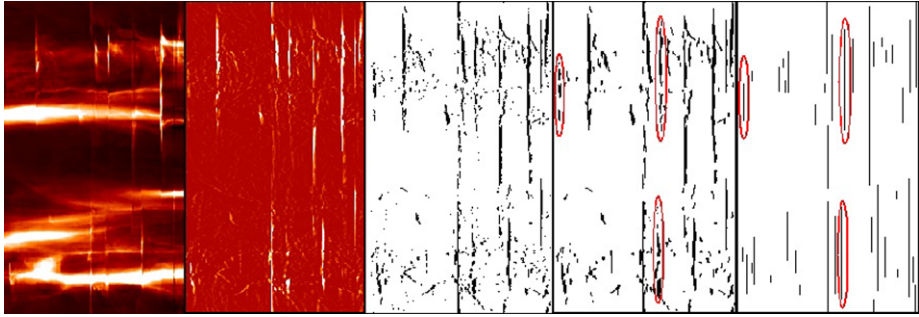
Figure 3 The four steps of the procedure applied to the original synoptic maps (left panel). From left to right: filtering, thresholding, segmentation, and merging with high-level knowledge. The effect of this final step is highlighted on three events with red ellipses. The rightmost image is the detection mask used when computing the propagation velocity. Each subimage extends over five days (x-axis) and 360° (y-axis).

- The filtering consists of subtracting a background K-corona obtained by applying a median filter to the original map with a horizontal window of six hours.
- The thresholding isolates the most significant structures and returns a 2D binary mask.
- The segmentation implements the line-adjacency graph (LAG) of Pavlidis (1986). It performs a morphological closure to eliminate artificial holes and identifies and labels regions of interests (ROI) with a list of parameters associated to each ROI, such as its geometric center and its area.
- The merging with high-level knowledge regroups disjoint ROIs if they appear to belong to the same CME based on several conditions, mainly temporal simultaneity. A mask is finally produced where every CME is represented by a vertical segment whose center is that of the final ROI, and whose vertical extent is its height (see last panel of Figure 3). Only CMEs with a minimum angular extent of 7° are kept. Masks obtained at different radial distances are used to determine the velocities.

The main difference of the new procedure from the previous one is the values of the numerical criteria that are used to adapt them to the new synoptic maps; in addition, several sections of the code were rewritten in a more efficient and robust way.

3.2. CME Parameters

3.2.1. Date and Time of Appearance, Position Angle, and Angular Width

These three parameters are determined during the segmentation of the synoptic maps and are written as parameters attached to each ROI. They are all estimated from the synoptic maps at a radial distance of 3 $R_\odot$. This is particularly important for the parameter "date and time of appearance" because other catalogs use different definitions. The first two parameters are estimated from the abscissa and ordinate of the geometric center of the ROI, thus giving the same weight to every pixel in that ROI. The angular width of a CME is given by the vertical extent of the ROI. These parameters are only little affected by the introduction of the new HD synoptic maps.

3.2.2. *Velocity*

As for ARTEMIS-I, our new catalog reports three velocities for each CME whenever their determination is successful, depending upon the visibility of the CME throughout the LASCO-C2 field-of-view.

First, an approximate value, called the propagation velocity, is calculated from the detection masks at each of the six selected solar distances. Starting at 3 $R_\odot$ taken as a reference, the signatures of a given CME are progressively shifted on the successive masks. Assuming a constant velocity between 50 and 2000 $km\,s^{-1}$ and sampling this interval with a step of 10 $km\,s^{-1}$, the shifts are calculated at each radial distance; the opposite shift is applied to the corresponding detection mask, so that a hypothetical CME with this velocity will appear located at 3 $R_\odot$. The masks obtained at different radial distances are then summed and the pixel value at the center of the CME corresponds to the number of masks that are consistent with the given velocity. The propagation velocity finally associated with a CME is the one that maximizes the number of matches, further requiring that there must be at least three matches. The determination of this propagation velocity serves as a filter ensuring that the CME has been detected on at least three synoptic maps, which allows us to proceed with more complex methods, for which it is used at a first estimate.

Improved determinations of the velocity are obtained by cross-correlating the detected CMEs on the original synoptic maps at 3 $R_\odot$ and 5.5 $R_\odot$. Two identical subimages encompassing the CME are extracted from the two maps: the first one at the location found at 3 $R_\odot$, and the second at the shifted location at 5.5 $R_\odot$ calculated with the propagation velocity. To reach subpixel accuracy in the horizontal correlation, each line of the two subimages is oversampled by spline interpolation by a factor of 100. A first correlation is performed on the two synthetic profiles obtained by summing all lines in each subimage; this yields the global, or mean, velocity of the CME. A second correlation is performed line by line and yields the velocity distribution as a function of polar angle and therefore provides information on its dispersion across the CME; the median value of the distribution provides the third estimate: the median velocity of the CME.

Determinations outside the range $50 - 2000$ $km\,s^{-1}$, or with a correlation coefficient below 0.5, are deemed unrealistic and ignored (they usually result from incorrect associations of different structures).

The procedures were partly rewritten to adapt them to the new HD maps. Several small corrections were additionally introduced and greatly improved our results: the percentage of successful determinations of the propagation velocity increased from 30 % (ARTEMIS-I) to 79 % (ARTEMIS-II); that of the global velocity from 23 % to 58 %, and that of the median velocity from 24 % to 78 %. In other words, our new catalog reports ≈ 2.5 times more velocities (which means that 2.5 times more CMEs are fully characterized, as we show below).

3.2.3. *Intensity*

The intensity parameter [I] was briefly introduced by Boursier *et al.* (2009), but was not implemented in the ARTEMIS-I automatic procedure. It quantifies the total radiance of a CME at 3 $R_\odot$ as the excess radiance over the background and is calculated by summing the pixel values of the filtered synoptic maps limited by the masks resulting from the segmentation and merging operations, that is

$$I = \sum_{j=1}^{p} \sum_{i=1}^{n} B(r, \theta_i, t_j). \tag{1}$$

The discrete summations result from the sampling of the synoptic maps at 3 $R_\odot$: p intervals of $\Delta t = 27$ minutes, and n sections of $\Delta_{\text{polar angle}} = 0.4°$. The background is calculated using a linear interpolation between the coronal signals recorded just before and just after the CME to account for the changes that the CME may induce on the corona.

While offering an estimate of the strength of a CME, this intensity does not strictly correspond to its total radiance as recorded on the original C2 images because of the incomplete sampling introduced by the synoptic maps. When comparing CMEs, it is furthermore biased by their velocities. Indeed, consider two identical CMEs in terms of radiance and size, but with different velocities, where the first one has twice that of the second one, for instance. The slowest CME will therefore appear in twice as many columns as the fast one, and the intensity of the former will be twice that of the latter.

As we show in the next section, we could conceivably correct for this effect by multiplying the intensity by the velocity. However, this would limit the determination of the intensity to about two-thirds of the CMEs in our catalog, and would also increase the uncertainty intrinsic to the calculation of the intensity by that from the velocity. Approximately 50 % of the CMEs have velocities in the range 200 to 450 km s^{-1}, so its effect is limited to a factor of about two for most of them. Therefore, we prefer to display the intensity as defined above since it is simply calculated from the observed radiance with a uniform procedure, but we emphasize that it is only an approximate estimate of the CME strength. It may also be viewed as a quality factor because the brightest CMEs recorded on the synoptic maps stand the best chance of being accurately characterized. The real quantitative criterion is the mass, whose determination (limited to CMEs with known velocity) is presented in the next section.

3.2.4. Mass

Based on the arguments presented in the previous section, the mass of a CME cannot be directly calculated from the radiance recorded on the synoptic maps, and estimating it correctly requires a more elaborate approach. This consists of considering a surface crossed by the whole CME and calculating the mass flow through it. This surface [$\mathcal{S}$] is defined as a cylinder whose axis is the line-of-sight to the Sun center and whose radius is $r = 3$ $R_\odot$. We also define a unit vector $\mathbf{n}$ normal to $\mathcal{S}$. We naturally introduce the cylindrical coordinates (r, θ, z), with the z-axis along the line-of-sight and origin $z = 0$ in the plane of the sky, r is the radial distance from the z-axis, and θ is the polar angle. The geometry is represented in Figure 4. We consider that any line originating from any point of a CME crossing $\mathcal{S}$ that is orthogonal to the plane of the sky can be assimilated to a line-of-sight.

Let $\rho(r, \theta, z, t)$ and $\mathbf{v}(\theta, z, t)$ be the surface mass density and the velocity vector of the CME as functions of time [t]. We explicitly assume that the velocity is independent of r and constant from 3 to 5.5 $R_\odot$, with a component v_n normal to $\mathcal{S}$ given by its global velocity as defined in Section 3.2.2. The velocities reported by the CDAW catalog confirm that they vary at most by 10 % in the above range of radial distances.

The mass [M] of the CME is the total mass flow through the surface $\mathcal{S}$ integrated over time,

$$M = \int_t \int_S \rho(\theta, z, t) \mathbf{v}(\theta, z, t) . \mathbf{n} \, \mathrm{d}z \, r \, \mathrm{d}\theta \, \mathrm{d}t$$

$$= v_n \int_t \int_S \rho(\theta, z, t) \, \mathrm{d}z \, r \, \mathrm{d}\theta \, \mathrm{d}t. \tag{2}$$

The integral of the mass density along the line-of-sight $\int_z \rho(\theta, z, t) \, \mathrm{d}z$ can be obtained from the observed radiance as explained below.

Figure 4 Geometry relevant for calculating the mass of a CME. The Sun is at S, the observed area is at M, and its projection on the plane of the sky is at P.
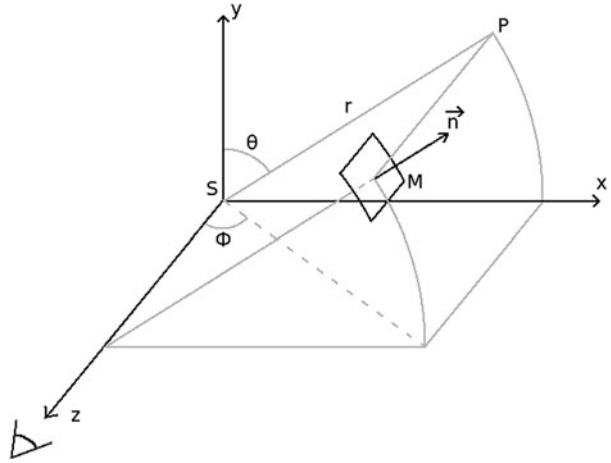
Following the formalism of Billings (1966), or the more rigorous revision recently performed by Howard and Tappin (2009), the K-corona radiance depends only upon the electron density [N_e], the scattering angle [ϕ], and the distance from the Sun center [R] (and is therefore different from the r introduced previously). These last two parameters can be expressed as functions of r and z via $\tan(\phi) = r/z$ and $R = r/\sin(\phi)$. This radiance integrated over the line-of-sight is therefore given by

$$B(r, \theta, t) = \int_z I_0 N_e(r, \theta, z, t) \frac{\pi \sigma}{2} C(R, \phi) \, dz, \tag{3}$$

with I_0 the radiance at the Sun center and σ the Thomson-scattering cross-section for a single electron [$\sigma = 7.95 \times 10^{-26}$ cm^2 sr^{-1}]. The dimensionless quantity C

$$C(R, \phi) = 2\big[(1 - u)c(R) + u d(R)\big] - \big[(1 - u)a(R) + u b(R)\big] \sin^2 \phi \tag{4}$$

expresses the light scattered by a volume of the corona depending upon its distance from the Sun center and the scattering angle; u is the limb-darkening coefficient; and a, b, c, and d are coefficients that only depend upon the distance from the Sun center. We consider that the CMEs have the standard composition used by Vourlidas *et al.* (2000), *i.e.* a completely ionized mix of 90 % hydrogen and 10 % helium, implying that to each free electron corresponds an element of the CME of mass $m_K = 1.97 \times 10^{-24}$ g, so that $\rho(r, \theta, z, t) = m_K N_e(r, \theta, z, t)$.

At this stage, we can only proceed if we make the usual assumption that the CME lies close to the plane of the sky, *i.e.* $\phi \approx 90°$ and $z \approx 0$. We emphasize that all published CME masses determined from LASCO images are based on this assumption, except for the few cases where the trajectory of the CME (and therefore its spatial localization) was reconstructed. Equation (3) then simplifies since $C(R, \phi)$ assumes its value in the plane of the sky,

$$B(r, \theta, t) = \frac{I_0 \pi \sigma C(r, 90)}{2 m_K} \times \int_z \rho(r, \theta, z, t) \, dz, \tag{5}$$

yielding,

$$\int_z \rho(r, \theta, z, t) \, dz = \frac{2 m_K B(r, \theta, t)}{I_0 \pi \sigma C(r, 90)}. \tag{6}$$

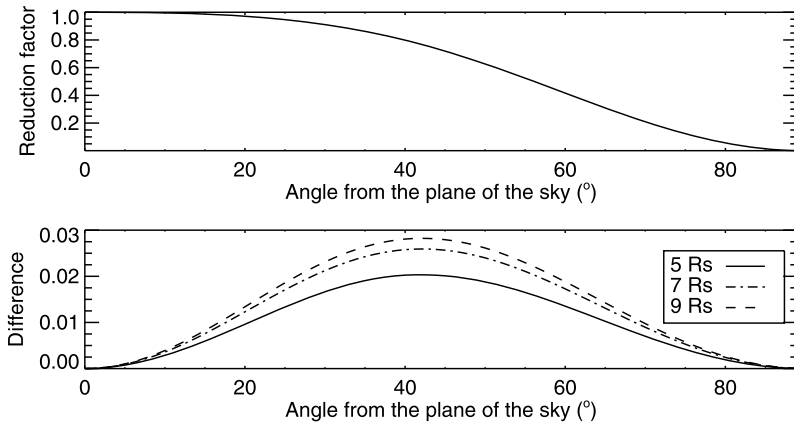Combining Equations (2) and (6) yields

Figure 5 Variation of the reduction factor that modifies the mass of CMEs as a function of their angle with the plane of the sky. The top panel displays the reduction factor corresponding to a distance of 3 $R_\odot$ as used in our method. The bottom panel displays the difference of the reduction factors at different distances, taking the curve at 3 $R_\odot$ of the top panel as reference.

$$M = \frac{2\,m_K v_n}{I_0 \pi \sigma C(r, 90)} \times \int_t \int_\theta B(r, \theta, t) r\, d\theta\, dt. \tag{7}$$

The double integral of $B(r, \theta, t)$ over time and polar angle may be expressed in terms of the intensity $[I]$ introduced in the previous section, and we finally obtain

$$M = \frac{2m_K v_n}{I_0 \pi \sigma C(r, 90)} \times I r\, \delta\theta\, \delta t. \tag{8}$$

In summary, we can therefore estimate the mass of all CMEs for which we can determine the velocity.

The mass of CMEs that significantly depart from the plane of the sky is underestimated by our procedure, the reduction factor increasing with the angle from that plane as displayed in Figure 5. This factor depends only very weakly on the heliocentric distance. Indeed, for a given value of this angle and as the distance varies, the mass of the in-plane CME and that of the corresponding out-of-plane CME follow identical variations so that the reduction factor remains practically constant. Second-order effects are present, but are very small, as can be seen in the bottom panel of Figure 5, which shows the differences at different distances with respect to the variation of the reduction factor at 3 $R_\odot$. The procedures that use the LASCO images themselves (such as implemented in the CDAW catalog) face the same problem, and in practice, their reduction factor is similar to ours since it is independent of the heliocentric distance, as discussed above.

3.2.5. Kinetic Energy

With both the mass and the velocity estimated, calculating the kinetic energy is straightforward via the usual formula $E = \frac{1}{2} M v_n^2$, and the results are listed in the catalog. We consider that the most appropriate velocity of the CME is the "global velocity", consistent with its use in the mass determination.
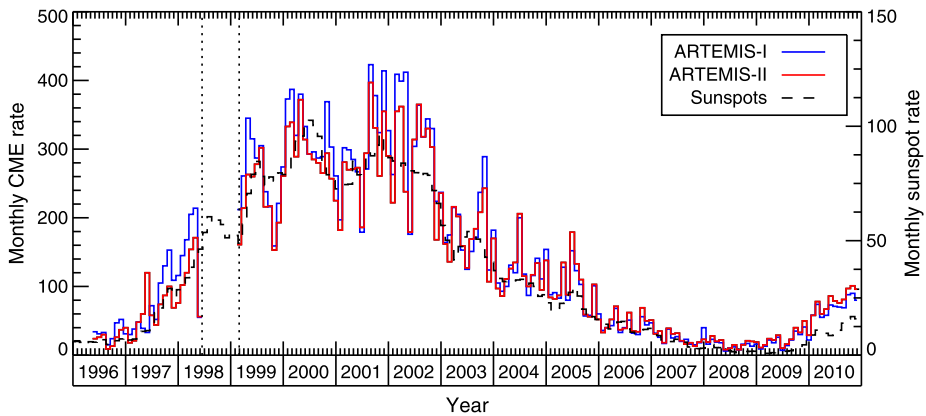
Figure 6 Monthly rates of CMEs reported by the ARTEMIS-I and ARTEMIS-II catalogs (left scale) to be compared with the smoothed monthly sunspot number (dashed line, right scale). The two vertical dotted lines delimit the data gap resulting from the loss of SOHO.

4. Results

We now first compare the results of ARTEMIS-II with those of ARTEMIS-I to assess the progress resulting from the introduction of the high-resolution synoptic maps, then we compare them with those of other catalogs to offer a broader perspective on the problem of CME detection and characterization.

4.1. Monthly Rate of CMEs

Figure 6 displays the monthly rates of CMEs reported by the ARTEMIS-I and -II catalogs from January 1996 to December 2010. They are very similar; the correlation between the two distributions reaches 0.98. Altogether, the first catalog lists 22 976 events, whereas the second lists 21 394 events, a difference of about 7 %. This may be explained by slight differences in the implementation, *e.g.* differences in the thresholds and in the segmentation parameters, and an improved merging of the CMEs, which are split between the top and bottom of the maps. Figure 6 furthermore confirms that the monthly rate of CMEs closely follows the pattern of solar activity, as illustrated by the sunspot number.

Moreover, the distributions of position angle and angular width are identical, which confirms that the two catalogs indeed detect the same population of CMEs and ensures that the statistical properties of the CMEs are maintained over 15 years.

4.2. Velocity of CMEs

4.2.1. Comparison of the ARTEMIS-I and ARTEMIS-II Catalogs

As emphasized in Section 3.2, the ARTEMIS-II catalog reports velocities for 2.5 times more CMEs than ARTEMIS-I: a substantial progress clearly resulting from the introduction of the new high-definition synoptic maps, but also from various improvements in the implementation of the procedure. Such a huge gain is beneficial to the statistical significance of our distributions.

Figure 7 displays the distributions of both the global and median velocities listed in our two catalogs. We note the similarity of the two global velocity distributions, meaning that the
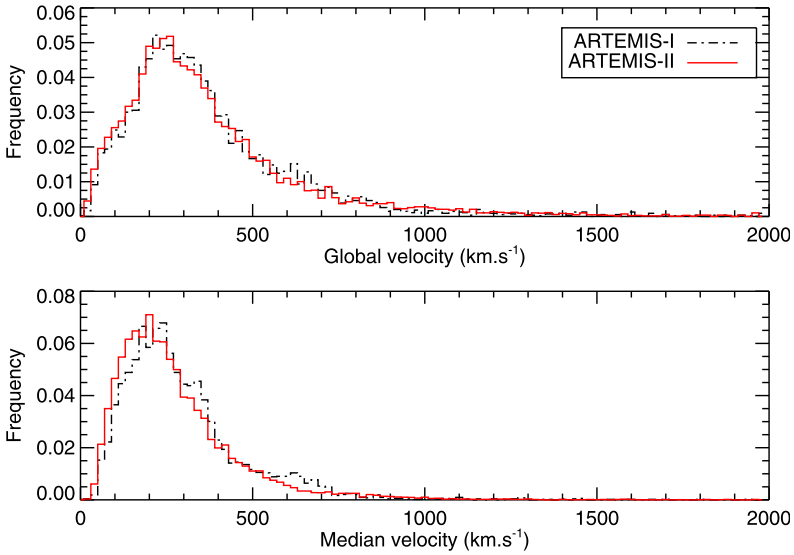
Figure 7 Normalized distributions of the global (upper panel) and the median (lower panel) velocities of CMEs listed in the ARTEMIS-I and -II catalogs. The bins have a width of 20 km s^{-1}.
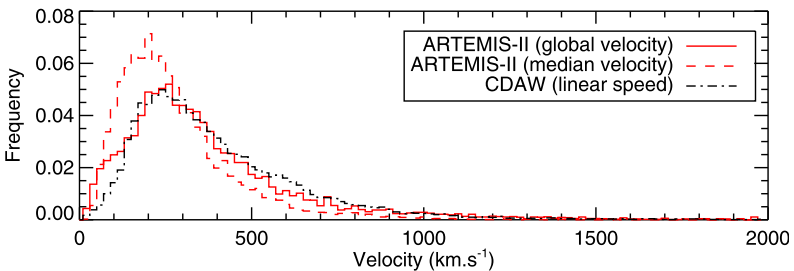

Figure 8 Normalized distributions of CME velocities listed in the ARTEMIS-II and CDAW catalogs.

limited set of CMEs with velocities reported in ARTEMIS-I was already fully representative of the whole population of CMEs. The distribution of median velocities in ARTEMIS-II is slightly shifted toward lower values by approximatively 15 %. This velocity involves the velocity variation across its latitudinal extent; the sides of the CMEs, which are generally slower than their front, are better handled by our new implementation, which most likely explains the above shift.

4.2.2. Comparison of ARTEMIS-II and Other Catalogs

Figures 8, 9, and 10 display the distributions of the linear speed reported in the CDAW, CACTus, and SEEDS catalogs compared with the ARTEMIS-II results. To properly understand these results, one should keep in mind several factors: First, the procedures are different: ARTEMIS and SEEDS use only LASCO-C2 images, whereas CDAW and CACTus use both C2 and C3 images. It is known that many CMEs accelerate/decelerate while crossing the C2 and C3 fields-of-view so that their linear speed reported in the CDAW and CACTus
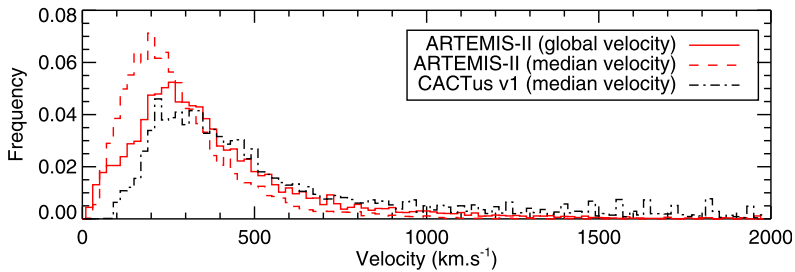
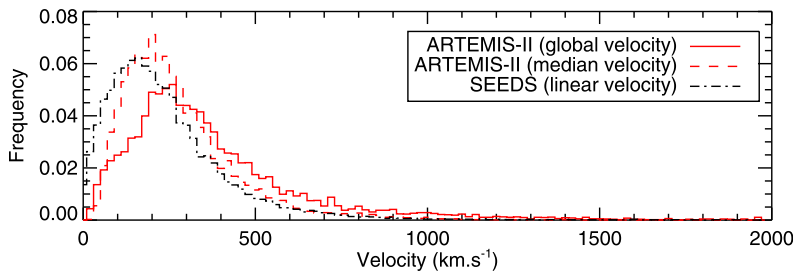**Figure 9** Normalized distributions of CME velocities listed in the ARTEMIS-II and CACTus catalogs.

Figure 10 Normalized distributions of CME velocities listed in the ARTEMIS-II and SEEDS catalogs.

catalogs may well differ from their velocity measured at low radial distances. However, as we discuss in more detail below, we did not observe a systematic bias between our global and the CDAW velocities (Figure 8). Second, a unique value for the velocity of a CME remains a simplistic view because different parts of the CME travel at different velocities, so that a velocity field would be a much more appropriate description (Boulade *et al.*, 1997; Robbrecht and Berghmans, 2004; Colaninno and Vourlidas, 2006). Generally speaking, the front part has the highest velocity, with the rear and side parts trailing behind. Our global velocity gives a higher weight to the brightest parts, that is the front and central parts (which are the fastest), whereas our median velocity gives an equal weight to every angular section of the CME. The CDAW linear speed is obtained by fitting a straight line to the height–time measurements made at the fastest section of CMEs, at the so-called measurement position angle (MPA). It is noted that the MPA does not always coincide with the central position angle (CPA), for instance in the case of CMEs that move non-radially. CACTus measures a linear speed profile as a function of the position angle over the CME angular width and lists the median value. The SEEDS speed is taken from the highest peak using the leading-edge segmentation.

Our distribution of global velocities and that of CDAW speeds are in excellent agreement, consistent with their general relevance to the fastest parts of the CMEs. The ARTEMIS-II distribution exhibits a bump for the slowest CMEs, probably corresponding to a population of faint CMEs that cannot be tracked by the CDAW procedure. The agreement is less satisfactory with the CACTus speeds. We had anticipated that because of the fairly similar velocity determinations, their distribution would match the ARTEMIS distribution of median velocities, but, surprisingly, this is not the case. In fact, a better agreement is achieved by our global velocities because the two distributions have their broad maxima in the same range. Apparently, CACTus is missing a substantial number of slow CMEs with veloci-
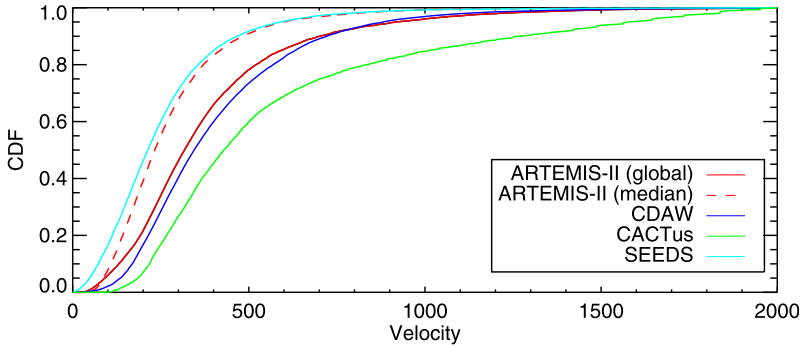
Figure 11 Cumulative distribution functions of the velocity of the CMEs listed in the four LASCO catalogs.

ties lower than about 300 km s^{-1} and has a cut-off at about 100 km s^{-1}. Curiously enough, CACTus reports a significant number of fast CMEs with velocities exceeding 1200 km s^{-1} that are not detected by the other three catalogs. The comparison with the SEEDS results is equally puzzling because we had anticipated an agreement with the ARTEMIS-II distribution of global velocities, but their distribution is far more consistent with the distribution of median velocities.

A synthetic comparison of the velocity distributions of the different catalogs is presented in Figure 11 in terms of the cumulative distribution functions (CDFs), which are less prone to artifacts associated with histograms (in contrast to histograms, CDFs are insensitive to the bin size as long as it is small enough). They confirm the above conclusions in a very clear way, in particular the large excess of fast CMEs reported by CACTus, and furthermore allow quantifying the differences between the distributions. We employed a Kolmogorov–Smirnov (K–S) test to quantify the probability [P_{KS}] that two distributions are drawn from the same parent distribution of CMEs, as they theoretically should be. The K–S test essentially measures the shift between two distributions and is most sensitive around the median values of the CDFs. We therefore quantified the differences between two distributions by progressively shifting one with respect to the other and calculating the K–S probability at each step. The shift that maximizes this probability is used as a measure of the difference between the two distributions. Using the ARTEMIS-II CDF of global velocities as a reference, we found differences of 29 km s^{-1} with CDAW, 126 km s^{-1} with CACTus, and 97 km s^{-1} with SEEDS. However, using the ARTEMIS CDF of median velocities reduces the difference with SEEDS to 27 km s^{-1}. We investigated whether these results could be biased by comparing slightly different populations of CMEs and therefore re-derived the CDFs in the restricted interval of velocity ranging from 100 to 1000 km s^{-1}. The top panel of Figure 12 confirms the main features observed in Figure 11, except that the removal of the slowest CMEs (< 100 km s^{-1}) brings the SEEDS and the ARTEMIS-II (median velocity) distributions in close agreement. We finally checked the influence of the angular width of the CMEs by distinguishing two intervals: $0 - 30°$ and $30 - 360°$. Here again, the two bottom panels of Figure 12 do not reveal any significant alterations of the above picture. Two minor effects may be noted, however: i) in the interval $0 - 30°$, the agreement between the SEEDS and the ARTEMIS-II (median velocity) distributions is quasi-perfect and ii) in the interval $30 - 360°$, the CDAW and the ARTEMIS-II (global velocity) distributions are very close and conspicuously closer even than in the other interval.
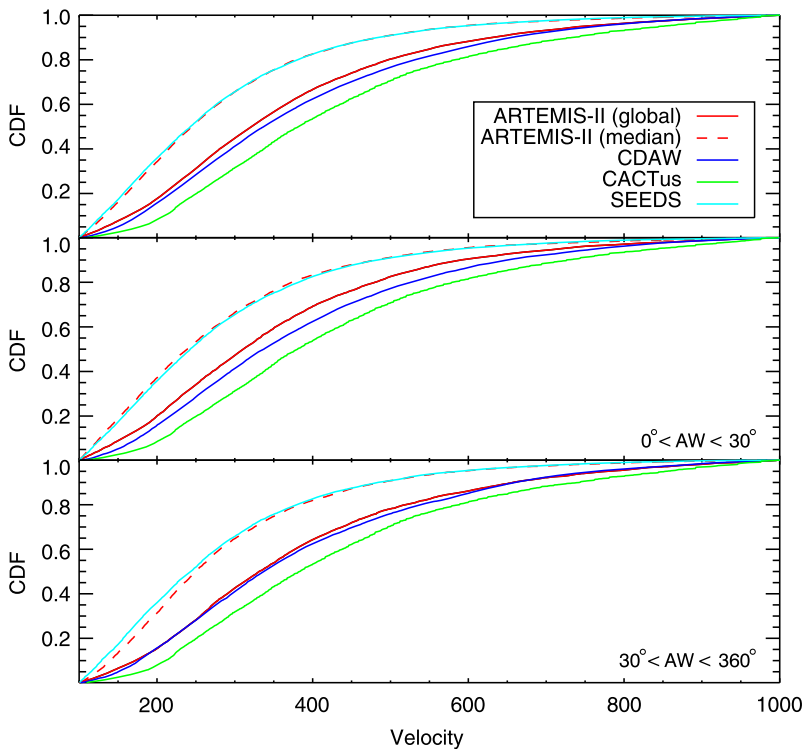
Figure 12 Cumulative distribution functions of the CME velocities listed in the four LASCO catalogs restricted to the interval 100 to 1000 km s^{-1}. The upper panel displays the results without a restriction on the CME angular width [AW]. The middle and lower panels display the results in two complementary domains of angular width: $0-30°$ and $30-360°$.

4.2.3. Comparison of the Catalogs with Three-Dimensional Reconstructions

We performed a final test of the velocity determination by considering the few CMEs for which a full three-dimensional reconstruction of their kinematics has been achieved thanks to stereographic observations performed with the SECCHI coronagraphs (Howard *et al.*, 2008). Thernisien, Vourlidas, and Howard (2009) used only SECCHI-COR2 and modeled twenty-six events, but only for twenty is the velocity listed in the ARTEMIS catalog; their velocities are relevant to a distance of approximately 10 R$_\odot$. Joshi and Srivastava (2011) used both the SECCHI-COR1 and -COR2 to study six events, but only five were used for comparison, because the sixth is undetected in all LASCO catalogs (as a consequence of a data gap). We extracted from their plots the true (unprojected) velocities averaged between 3 and 5.5 R$_\odot$ to be consistent with the ARTEMIS determinations. The two sets of results (which have two CMEs in common) together with the values listed in the four LASCO catalogs (with the exceptions of a few events that could not be identified or had no velocity estimation) are presented in Table 1. For the modeled CMEs, we also indicate in parenthesis the projected velocities using the angles determined by Thernisien, Vourlidas, and Howard (2009). The angles for four of the Joshi and Srivastava (2011) CMEs are not known, and we assumed that their projected velocities are equal to their true velocities. This is probably not valid for two of these CMEs because they are seen on both limbs on COR2-A and -B,

Table 1 Properties of the CMEs reconstructed by Thernisien, Vourlidas, and Howard (2009) and Joshi and Srivastava (2011) identified in the ARTEMIS-II catalog. The angle determined by Thernisien, Vourlidas, and Howard (2009) is measured between the CME center and the LASCO plane of the sky. Projected velocities [V_p; km s^{-1}] from the four LASCO catalogs are to be compared with the velocities obtained from the reconstructions and with the projected velocities recalculated when the CME angle is known (given in parenthesis). A subset of these CMEs have mass [g] estimates from Colaninno and Vourlidas (2009) and are compared with the masses in the ARTEMIS and CDAW catalogs when available. The recalculated "projected masses" are given in parenthesis, likewise the projected velocities above.

Date ARTEMIS	Angle	V_p ARTEMIS	V_p CDAW	V_p SEEDS	V_p CACTus	V (V_p) Thernisien	V (V_p) Joshi	Mass ARTEMIS	Mass CDAW	Mass Colaninno
s 04-Nov-2007 13:15	46	159	179	110	180	216 (150)		6.6×10^{13}	3.0×10^{15}	
s 16-Nov-2007 12:23	33	192	326	160	213	345 (289)	240 (201)	9.6×10^{14}	2.5×10^{15}	
s 04-Dec-2007 07:06	19	111	210	96	328	265 (251)		1.3×10^{15a}	8.1×10^{15}	2.6×10^{15} (2.5×10^{15})
s 16-Dec-2007 13:41	54	133	184	145	143	325 (191)		2.3×10^{13}	4.5×10^{15}	
s 31-Dec-2007 02:27	10	599	995	486	741	972 (957)	712 (701)	8.4×10^{15}		7.7×10^{15} (7.7×10^{15})
s 02-Jan-2008 11:58	39	402	676	350	411	731 (568)		5.0×10^{15}		5.3×10^{15} (4.5×10^{15})
s 23-Jan-2008 01:50	70	157	362	181	195	442 (151)		6.9×10^{14}		
s 29-Jan-2008 19:19	17	210	168	248	223	246 (235)		1.5×10^{14}	3.7×10^{13}	
s 12-Feb-2008 08:39	3		266	47	178	249 (249)			3.5×10^{15}	4.5×10^{15} (4.5×10^{15})
s 13-Feb-2008 15:11	72	51	157			225 (70)		1.2×10^{14}		
s 15-Feb-2008 06:24	17	103	163	102	215	230 (220)		3.7×10^{14}	2.7×10^{15}	3.2×10^{15} (2.9×10^{15})
s 24-Feb-2008 11:07	32	208	246	93	358	244 (207)		5.1×10^{13}	3.2×10^{15}	
s 17-Mar-2008 10:14	50	124	211	107	183	221 (142)		9.1×10^{13}	8.3×10^{14}	
s 25-Mar-2008 20:32	7	640	1103	337	880	1127 (1119)		3.2×10^{15}		2.9×10^{15} (2.9×10^{15})
s 05-Apr-2008 17:21	36	656	962	591	781	1043 (843)		2.5×10^{15}		2.8×10^{15} (2.4×10^{15})
s 09-Apr-2008 11:55		371	650	354	430		420	1.0×10^{15}	1.4×10^{15}	
s 26-Apr-2008 16:03	69	363	515	461	383	741 (266)		1.0×10^{15}		
s 17-May-2008 11:52	45	784	630	694	631	986 (697)		6.1×10^{14}		2.8×10^{15} (6.4×10^{14})
s 12-Jun-2008 07:09	12	148	274	134	218	319 (312)		1.5×10^{15}	1.6×10^{15}	
s 26-Jun-2008 04:45	57	174	204	154	216	389 (212)		3.4×10^{14}	8.2×10^{14}	
s 07-Jul-2008 17:17	67	174		193	160	292 (114)		2.1×10^{14}		
s 31-Jul-2008 18:16	51	106	164	136	165	288 (181)		5.3×10^{14}	7.5×10^{14}	
s 16-Dec-2009 05:51		193	276		221		313	2.1×10^{14}		
s 13-Apr-2010 11:46		269	452	208	383		313	2.8×10^{15}	4.9×10^{15}	

[a]This mass is the sum of the masses of two events that successively occurred on 04-Dec-2007 at 07:06 and 10:00 (see text for details).
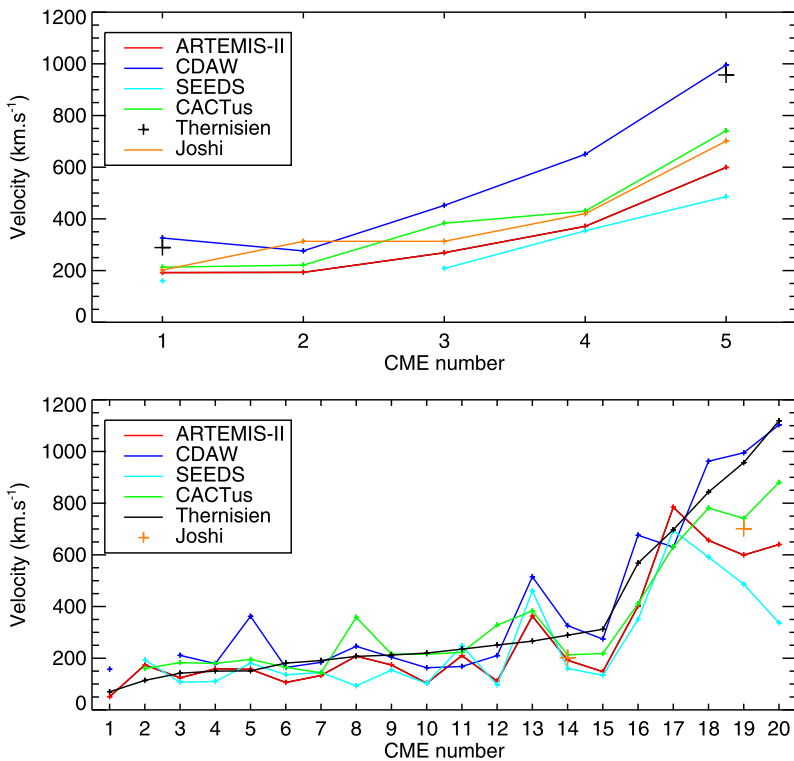
Figure 13 Projected velocities of CMEs modeled by Thernisien, Vourlidas, and Howard (2009) and Joshi and Srivastava (2011) compared with the four LASCO catalogs. The lower panel is based on the 20 velocities reported in the first reference and ordered by increasing values. The upper panel is based on the five velocities reported by Joshi and Srivastava (2011) and ordered in increasing values.

suggesting a large angle from the plane of the sky, and therefore much lower projected velocities. Figure 13 illustrates these results by comparing the projected velocities of the modeled CMEs with those listed in the four catalogs. In the two panels of this figure, we assigned arbitrary numbers to these CMEs ordered by increasing velocity values to allow a simple and legible presentation of these results.

Considering first the results of Joshi and Srivastava (2011), one sees that the ARTEMIS-II and CACTus determinations perform extremely well. This is also the case for CDAW for the first three CMEs, but not for CMEs 4 (9 April 2008) and 5 (31 December 2007), see upper panel of Figure 13, for which it reports much higher velocities. The velocity profile of CME 4 in the CDAW catalog indicates a slight acceleration that cannot explain the above difference, which therefore could result from the selection of the MPA in CDAW, *i.e.* the fastest point. According to Joshi and Srivastava (2011), the velocity profile of CME 5 is quite complex, with successive phases of acceleration and deceleration. At the distances relevant to the different catalogs, this profile indicates ≈ 700 km s^{-1} for ARTEMIS-II (to be compared with the listed value of ≈ 600 km s^{-1}) and ≈ 900 km s^{-1} for CDAW (to be compared with the listed value of 1000 km s^{-1}), which explains most of the difference. Beyond ≈ 6 R$_\odot$, this profile indicates a constant velocity, whereas CDAW measures a slight deceleration, but the two solutions lead to a range of 900 to 1000 km s^{-1} at ≈ 15 R$_\odot$, which

agrees well with the determination of Thernisien, Vourlidas, and Howard (2009). SEEDs tends to report lower velocities, consistent with the trend noted previously.

Turning now to the results of Thernisien, Vourlidas, and Howard (2009), the four catalogs perform well for the first twelve CMEs, with ARTEMIS achieving the lowest absolute and quadratic deviations (using the results of Thernisien, Vourlidas, and Howard (2009) as reference values) after CACTus. CME 13 (26 April 2008) in the lower panel of Figure 13 is somewhat of an exception, with all catalogs reporting higher velocities than the determination from the model. It departs significantly from the SOHO plane of the sky [69°] and lies within a few degrees of the line-of-sight of one of the COR2; these two circumstances probably lead to substantial uncertainties.

Starting with CME 14, but with the notable exception of CME 17, all catalogs except CDAW report velocities conspicuously lower than those of Thernisien, Vourlidas, and Howard (2009). The CDAW catalog indicates that CMEs 14, 15, and 16 have accelerated beyond 3 $R_{\odot}$, leading to higher velocities at the larger distances of the last two references. Conversely, CMEs 18, 19, and 20 are reported to have decelerated. However, these fast CMEs only appear in a few LASCO images, and this situation poses an extra challenge to the automatic detections. This is particularly the case of ARTEMIS, and we emphasize that the accuracy of the fastest CMEs is limited by the temporal resolution of our synoptic maps. Finally, for CME 19 (31 December 2007), Joshi and Srivastava (2011) reported a lower velocity than Thernisien, Vourlidas, and Howard (2009) and CDAW, in fact intermediate between the ARTEMIS and CACTus determinations.

4.3. CME Mass

Before comparing the results of ARTEMIS-II and CDAW (the only catalog that reports the CME mass), we briefly recall the CDAW method, which directly relies on the LASCO images, whereas ARTEMIS-II relies on synoptic maps. Following radiometric calibration, an image obtained just prior to the appearance of the CME is subtracted; this removes the background F-corona, static K-corona, and any residual stray light, and therefore yields the radiance of the CME. The total number of electrons along a given line-of-sight (as defined by a pixel) is given by the ratio of the radiance in that pixel to the radiance produced by a single electron assumed to be located in the plane of the sky. To convert the electron density to mass, the ejected material is considered to be a completely ionized mix of 90 % hydrogen and 10 % helium.

Figure 14 displays the distribution of the CME mass as determined by the ARTEMIS-II procedure together with that obtained from the CDAW catalog. On the one hand, the agreement for the upper quarter of the populations with the largest masses ($\geq 1 \times 10^{15}$ g) is excellent; the ARTEMIS values exceed the CDAW values by a factor ≈ 1.4, which is quite negligible in view of the different assumptions inherent to the calculations. On the other hand, ARTEMIS identifies a much larger population of CMEs at smaller masses ($\leq 1 \times 10^{15}$ g). Globally, the averages of the two distributions are almost the same (1.16×10^{15} g for ARTEMIS and 1.29×10^{15} g for CDAW), but this results from the weight of the most massive CMEs in the distributions. This does not mean that the two catalogs report the same mass for a given CME, however. There is a slight trend at very low masses ($\leq 2 \times 10^{13}$ g) with CDAW listing more events than ARTEMIS; this trend appeared only recently, however, as illustrated in Figure 15. This is a direct consequence of the emergence of a population of faint CMES during the declining phase of Solar Cycle 23 that were registered in the CDAW catalog. This causes the number of CDAW CMEs, which was about two thirds of the ARTEMIS number in the previous period, to equal and later exceed it. As a consequence, whereas the ARTEMIS mass distribution during the whole 1996 – 2010 period and
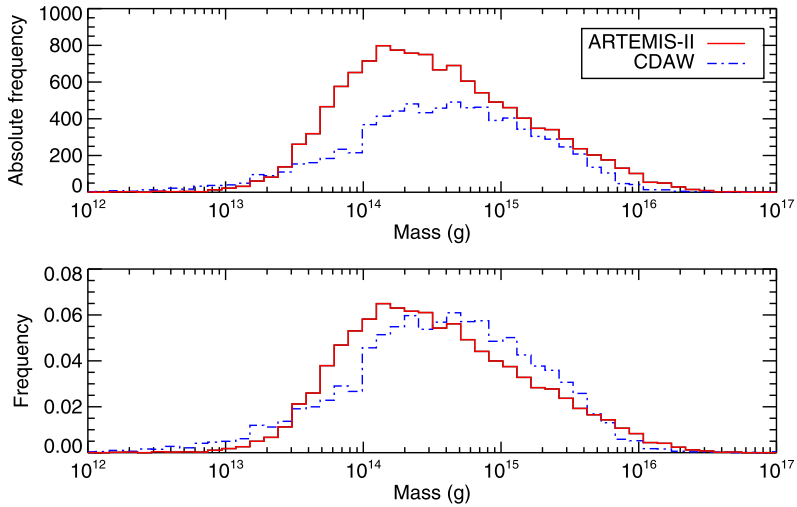
Figure 14 Distributions (top panel) and normalized distributions (lower panel) of the mass of CMEs derived from the ARTEMIS-II and CDAW catalogs.
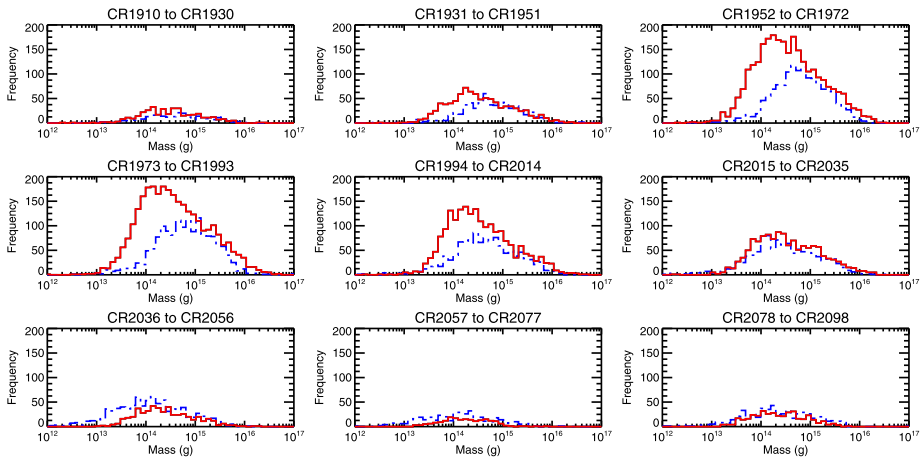

Figure 15 Distributions of the CME mass in successive periods of 15 Carrington rotations derived from the ARTEMIS-II (red line) and CDAW (dashed black line) catalogs.

that of CDAW before 2005 retain their respective shape over time and mostly evolve in amplitude, the CDAW distribution shifts toward lower values later on. As already pointed out by Boursier *et al.* (2009), the trend of CDAW to detect a constant rate of CMEs starting in December 2004, and even a slight increase, thereafter is not at all supported by the three automatic catalogs. It is even quite puzzling because these three catalogs are performing extremely well and agree on a decreasing rate of CMEs closely following the evolution of the sunspot number. The extra number of CDAW CMEs during the declining phase of activity, many of them labeled "poor events", are most likely artifacts of the visual detection. As a final remark, whereas the mass estimates are statistically quite similar, the comparison of a
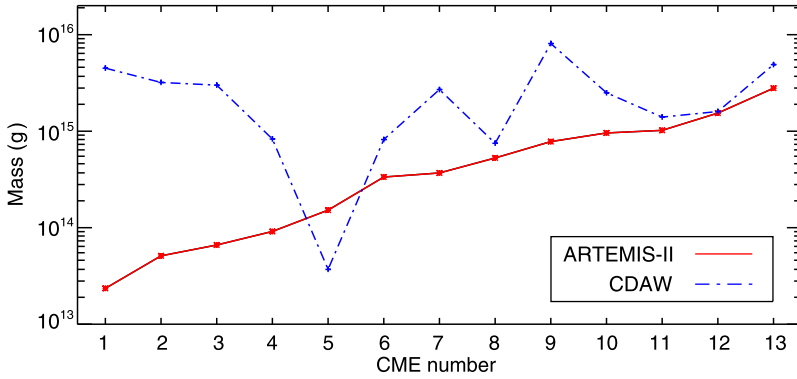
Figure 16 Comparison of the masses reported by the ARTEMIS-II and CDAW catalogs for the CMEs modeled by Thernisien, Vourlidas, and Howard (2009) ordered by increasing values of the ARTEMIS-II mass.
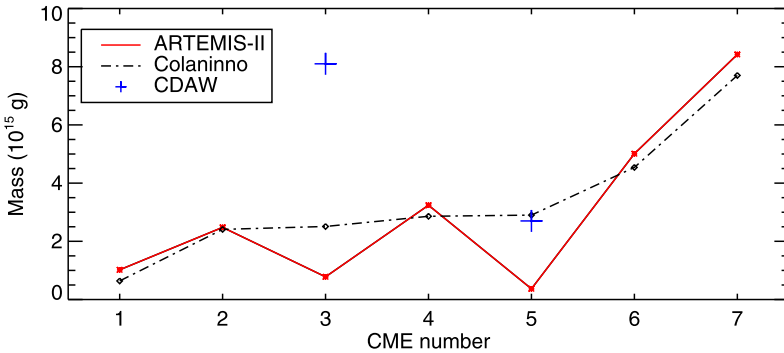
Figure 17 Comparison of the masses of the seven CMEs modeled by Colaninno and Vourlidas (2009) with the ARTEMIS-II and CDAW estimations ordered by increasing values of the Colaninno mass.

few individual values reveals that differences between the two catalogs may reach several orders of magnitude (Figure 16).

Finally, we considered the few CMEs with a reliable mass determination in the same way as the velocities. This has been achieved for eight events reported by Colaninno and Vourlidas (2009), exploiting the two independent views offered by the SECCHI coronagraphs of the STEREO mission. Their method is similar to that implemented by CDAW, except that the direction of propagation is left as a free parameter determined by imposing the constraint that the same mass should be derived from the two stereoscopic views. These eight CMEs are included in Table 1 and are generally close to the plane of the sky when observed by LASCO, so that the real angle has little impact on the mass determinations except for the last one. The masses reported by Colaninno and Vourlidas (2009), ARTEMIS, and CDAW (when available) are plotted in Figure 17 for better legibility. We also scaled the original masses of Colaninno and Vourlidas (2009) assuming that the CMEs lie in the plane of the sky (*i.e.* as seen by LASCO) using the correction factors of Figure 5; these scaled values appear in parenthesis in Table 1.

Unfortunately, two gaps in the LASCO data prevented us from estimating the mass of the 12 February 2008 event (which limits the comparison to seven CMEs) and made our es-

timation of the 15 February 2008 event uncertain (CME 5 in Figure 17). There is a different problem with the 4 December 2007 CME (CME 3), which is split into two events because the dimmer area between the CME's front and its core is unusually sharp on the synoptic maps. However, this case is easily corrected by summing the two events. Very few CMEs in the catalog are close enough in time and polar angle to potentially display this artifact.

The agreement between the SECCHI and ARTEMIS determinations for CMEs 1, 2, 4, 6, and 7 is quite impressive considering that the measurements are performed with different instruments and different techniques. ARTEMIS underestimates the mass of CME 3 (4 December 2007) by a factor $\approx$ two, probably because it was only imperfectly detected (split event as mentioned above). The discrepancy affecting CME 5 (15 February 2008) is not really significant; as we pointed out, the ARTEMIS determination is uncertain owing to a data gap.

5. Conclusions

Following the elaboration of a new set of high-resolution synoptic maps of the K-corona that takes fully advantage of the temporal cadence of the LASCO-C2 images, we have adapted our method of detecting and characterizing coronal mass ejections previously implemented in our first-generation ARTEMIS-I catalog and produced a second-generation ARTEMIS-II catalog. The most valuable improvement is the large increase of the number of CMEs for which we could determine the global velocity ($\approx 13\,000$ until December 2010), a gain of a factor ≈ 2.5, that is 58 % of the total number of cataloged CMEs. Finally, we developed a new procedure to estimate the mass (and kinetic energy) of the CMEs from their radiance recorded on the synoptic maps at 3 $R_\odot$. Our procedure is constrained by the usual assumption that the CMEs are close to the plane of the sky and limited to CMEs whose velocity is determined. In the same way as for the velocity, the mass and kinetic energy are estimated for 58 % of the total number of CMEs listed in the ARTEMIS-II catalog. A comparison with the results of other catalogs of LASCO CMEs revealed diverse trends. Globally, the distributions of velocities and masses reported by the CDAW and ARTEMIS-II catalogs agree well, but to some extent this hides a more complex situation; marked differences appear when the comparisons are restricted to individual events or to limited periods of time spanning the solar cycle. Compared with these two catalogs, the CACTus distribution presents a marked excess of high velocities, whereas the SEEDS distribution is systematically shifted to lower velocities, but agrees well with the ARTEMIS-II distribution of *median* velocities. Individual comparisons of velocities of 23 CMEs for which a full three-dimensional kinematic solution has been published indicate that ARTEMIS-II performs extremely well except at the highest velocities: an intrinsic limitation of our method. Finally, individual comparisons of mass determination of seven CMEs, for which a robust solution has been obtained from stereographic observations, demonstrate the excellent quality of the ARTEMIS-II results, although some local discrepancies may occur, an inevitable consequence of an automatic procedure. We are therefore confident that the ARTEMIS-II catalog accurately reports the properties of the thousands of CMEs recorded by LASCO, opening the way to an in-depth statistical analysis of their properties over more than a solar cycle; this will be the subject of a forthcoming article.

References

Billings, D.E.: 1966, *A Guide to the Solar Corona*, Academic Press, San Diego, 144 – 155. doi:10.1063/1.3034941.

Boulade, S., Delanné, C., Koutchmy, S., Lamy, P., Llebaria, A., Howard, R., *et al.*: 1997, Analysis of a high latitude slow CME with travelling ejecta. In: Wilson, A. (ed.) *Fifth SOHO Workshop: The Corona and Solar Wind Near Minimum Activity*, *ESA* **SP-404**, 217 – 221. ADS:1997ESASP.404..217B.

Boursier, Y., Lamy, P., Llebaria, A., Goudail, F., Robelus, S.: 2009, The ARTEMIS catalog of LASCO coronal mass ejections. *Solar Phys.* **257**, 125 – 147. ADS:2009SoPh..257..125B, doi:10.1007/s11207-009-9370-5.

Brueckner, G.E., Howard, R.A., Koomen, M.J., Korendyke, C.M., Michels, D.J., Moses, J.D., *et al.*: 1995, The Large Angle Spectroscopic COronagraph (LASCO). *Solar Phys.* **162**, 357 – 402. ADS:1995SoPh..162..357B, doi:10.1007/BF00733434.

Colaninno, R.C., Vourlidas, A.: 2006, Analysis of the velocity field of CMEs using optical flow methods. *Astrophys. J.* **652**, 1747 – 1754. ADS:2006ApJ...652.1747C, doi:10.1086/507943.

Colaninno, R.C., Vourlidas, A.: 2009, First determination of the true mass of coronal mass ejections: a novel approach using the two STEREO viewpoints. *Astrophys. J.* **698**, 852 – 858. ADS:2009ApJ...698..852C, doi:10.1088/0004-637X/698/1/852.

Howard, R.A., Moses, J.D., Vourlidas, A., Newmark, J.S., Socker, D.G., *et al.*: 2008, Sun Earth connection coronal and heliospheric investigation. *Space Sci. Rev.* **136**, 67 – 115. ADS:2008SSRv..136...67H, doi:10.1007/s11214-008-9341-4.

Howard, T.A., Tappin, S.J.: 2009, Interplanetary coronal mass ejections observed in the heliosphere: 1. Review of theory. *Space Sci. Rev.* **147**, 31 – 54. ADS:2009SSRv..147...31H, doi:10.1007/s11214-009-9542-5.

Joshi, A.D., Srivastava, N.: 2011, Acceleration of coronal mass ejections from three dimensional reconstruction of STEREO images. *Astrophys. J.* **739**, 739-8. ADS:2011ApJ...739....8J, doi:10.1088/0004-637X/739/1/8.

Lamy, P., Llebaria, A., Quemerais, E.: 2002, Solar cycle variation of the radiance and the global electron density of the solar corona. *Adv. Space Res.* **29**, 373 – 378. ADS:2002AdSpR..29..373L, doi:10.1016/S0273-1177(01)00599-3.

Olmedo, O., Zhang, J., Wechsler, H., Borne, K., Poland, A.: 2005, Solar eruptive event detection system (SEEDS). *Bull. Am. Astron. Soc.* **37**, 1342. ADS:2008SoPh..248..485O. doi:10.1007/s11207-007-9104-5.

Olmedo, O., Zhang, J., Wechsler, H., Poland, A., Borne, K.: 2008, Automatic detection and tracking of coronal mass ejections in coronagraph time series. *Solar Phys.* **248**, 485 – 499. ADS:2008SoPh..248..485O, doi:10.1007/s11207-007-9104-5.

Pavlidis, T.: 1986, A vectorizer and feature extractor for document recognition. *Comput. Vis. Graph.* **35**, 111 – 127. doi:10.1016/0734-189X(86)90128-3.

Qu, M., Shih, F.Y., Jing, J., Wang, H.: 2006, Automatic detection and classification of coronal mass ejections. *Solar Phys.* **237**, 419 – 431. ADS:2006SoPh..237..419Q, doi:10.1007/s11207-006-0114-5.

Robbrecht, E., Berghmans, D.: 2004, Automated recognition of coronal mass ejections (CMEs) in near-real-time data. *Astron. Astrophys.* **425**, 1097 – 1106. ADS:2004A&A...425.1097R, doi:10.1051/0004-6361:20041302.

Robbrecht, E., Berghmans, D., Van der Linden, R.A.M.: 2009, Automated LASCO CME catalog for solar cycle 23: are CMEs scale invariant? *Astrophys. J.* **691**, 1222. ADS:2009ApJ...691.1222R. doi:10.1088/0004-637X/691/2/1222.

Saez, F., Llebaria, A., Lamy, P., Vibert, D.: 2007, Three-dimensional reconstruction of the streamer belt and other large-scale structures of the solar corona. I. Method. *Astron. Astrophys.* **473**, 265 – 277. ADS:2007A&A...473..265S, doi:10.1051/0004-6361:20066777.

Thernisien, A., Vourlidas, A., Howard, R.A.: 2009, Forward modelling of coronal mass ejections using STEREO-SECCHI data. *Solar Phys.* **256**, 111 – 130. ADS:2009SoPh..256..111T, doi:10.1007/s11207-009-9346-5.

Tousey, R., Howard, R.A., Koomen, M.J.: 1974, The frequency and nature of coronal transient events observed by OSO-7. *Bull. Am. Astron. Soc.* **6**, 295. ADS:1974BAAS....6V.295T.

Vourlidas, A., Subramanian, P., Dere, K.P., Howard, R.A.: 2000, Large angle spectrometric coronagraph measurements of the energetics of coronal mass ejections. *Astrophys. J.* **534**, 456 – 467. ADS:2000ApJ...534..456V, doi:10.1086/308747.